Journal of Materials Chemistry C

How to realize spin-Seebeck effect with high spin figure of merit in magnetic boron-nitrogen nanoribbon and nanotube structures?

Journal:	*Journal of Materials Chemistry C*
Manuscript ID	TC-ART-07-2018-003560.R1
Article Type:	Paper
Date Submitted by the Author:	20-Aug-2018
Complete List of Authors:	Wu, Dan-Dan; Huazhong University of Science and Technology, School of Physics Fu, Huahua; Huazhong University of Science and Technology, School of Physics Liu, Qing-Bo; Huazhong University of Science and Technology, School of Physics Wu, Ruqian; UC Irvine ,

SCHOLARONE™
Manuscripts

Journal of Materials Chemistry C

PAPER

Cite this: DOI: 10.1039/xxxxxxxxxx

How to realize spin-Seebeck effect with high spin figure of merit in magnetic boron-nitrogen nanoribbon and nanotube structures?†

Dan-Dan Wu,[a] Hua-Hua Fu,*[ab] Qing-Bo Liu,[a] and Ruqian Wu*[b]

Received Date
Accepted Date

DOI: 10.1039/xxxxxxxxxx

www.rsc.org/journalname

The spin-Seebeck effect (SSE) has been regarded as one of core topics in spin caloritronics. To realize the SSE together with high spin thermoelectric conversion efficiency (TCE), two nanoscale structures referred to as nanoribbons and nanotubes have long been regarded as potential candidates. To illustrate their advantages to the above end, we construct magnetic boron-nitrogen nanoribbons (BNNRs) and nanotubes (BNNTs) by substituting some B atoms with carbon, and the BNNTs can be rolled from the BNNRs. To unify the magnetism origins, the edge magnetisms in BNNRs are cancelled by hydrogen passivation. Our theoretical results show that although these two different structures display similar spin semiconducting states, the BNNRs have lower lattice thermal conductance due to the phonon scattering in edges, contributing to the enhancement of spin figure of merit; while the BNNTs can generate better SSE and larger spin thermopower, due to the rotational symmetry. Moreover, we remove the hydrogen passivation from the BNNRs to construct another typical class of magnetic BNNRs, the electronic state in which is changed to the magnetic metallic one, which suppresses the spin thermopower and the SSE largely. The systemic and comparative studies help us to choose feasible routes to improve and design the SSE with high spin figure of merit in nanoscale structures, and give us deep understandings into the device applications of spin caloritronics based on the nanoribbon and nanotube materials.

1 Introduction

The spin Seebeck effect (SSE), as one of core topics in spin caloritronics, refers to the generation of spin voltage by a temperature gradient without any electronic bias in the ferromagnetic insulators or devices.[1–5] In recent decades, this thermo-spin effect has inspired tremendous research attentions, because it brings us a new energy-efficient conversion technology.[6,7] It is well established that the SSE can be occurred on the basis of either the spin-wave spin current or the conduction-electron spin current[8–11]. In the latter case, the spin currents are generated by the thermal electrons with opposite flow directions in the different transport channels with opposite spin directions.[12–16] With the recent development of nanotechnologies, we have found that the quantum materials with the structures of nanoribbons or nanotubes possess large thermoelectric conversion efficiency (TCE),[17,18] due to the outstanding quantum confinement effect.[19–23] To drive these structures to generate the SSE, a key condition is to obtain spin-dependent transport channels in materials. This requires some feasible means, such as magnetic-atom doping,[24–27] diverse defects,[28] function adsorbing[29] and edge reconstruction,[30,31] to modify the magnetic structures of nanoribbons and nanotubes. Moreover, to realize the SSE together with high spin figure of merit or the spin TCE, an urgent need is suggested to demonstrate the perspective advantages and disadvantages of the nanoribbons and the nanotubes constructed on the same quantum materials possessing the same magnetic origins.

We well know that hexagonal boron nitride (*h*-BN) is an sp^2-bonded layered van der Waals material with a structure similar to graphite.[32] The *h*-BN in monolayer form, similar to graphene, is semiconducting with wide and direct band gap of 5.9 eV,[33] and shows excellent chemical and thermal stability. Due to the novel electronic structures, this material has promising applications in photoluminescence, integrated circuits, lithium ion batteries, spintronics and vallytronics.[34–37] In this work, we construct the single-layer BN nanoribbons (BNNRs) and the single-walled BN nanotubes (BNNTs), which are prominent quasi-one-dimensional BN structures defined geometrically as thin strips of BN and cylindrical tubes, respectively. These two structures are intimately related, since BNNRs can be regarded as (or produced from) unrolled BNNTs. Moreover, the reduced dimensionality and

[a] *School of Physics, Huazhong University of Science and Technology, Wuhan 430074, People's Republic of China.*
[b] *Department of Physics and Astronomy, University of California, Irvine, California 92697-4575, USA.*
* E-mail: hhfu@hust.edu.cn (HF) and wur@uci.edu (RW)

screening of narrow BNNRs and small radius BNNTs may lead to high TCE.[38,39] To unify the magnetism origins, equal number of B atoms in every unit cell in both structures are substituted by carbon atoms to produce spin polarization. Meanwhile, to cancel the influence of the edge magnetism in the BNNRs, both edges in them are passivated by hydrogen atoms. Through calculating thermally driven spin currents, spin (charge) thermopowers, spin-dependence conductances, electric (phonon) thermal conductance, charge (spin) figure of merit and other thermoelectric parameters, we illustrate the respective advantages and disadvantages of the magnetic BNNTs and BNNRs towards the thermospin device applications in detail. The symmetric and comparative studies uncover that the rotational symmetry in nanotubes contributes to the SSE with the symmetrical spin currents, while the phonon scattering in the boundaries of nanoribbons decreases the phonon thermal conductance. These typical characters in structure influences their thermospin effects and the spin TCE largely. Additionally, we remove the hydrogen passivation from the BNNRs to construct another kind of BNNRs, and find some practical rules of the SSE in these two different nanoribbons. These theoretical results on the SSE enrich the field of spin caloritronics in the low-dimensional systems, and give us deep understandings into the nanoribbons and the nanotubes in the thermal spin device applications.

The remainder of this paper is organized as follows. In the Section 2, we design the BNNTs and two kinds of the BNNRs, and introduce the theoretical methods to calculate the thermal spin currents and various spin-dependent thermoelectric parameters. In the Section 3, we present the numerical results and discussion. Finally, some conclusions and summaries are given in the last section.

2 Device designs and theoretical method

We first construct three thermal spin devices based on a magnetic BNNT and two kinds of magnetic BNNRs. The BNNT is constructed based on the armchair (5,5)-BNNT as shown in Fig. 1(a), and the two BNNRs are structured on the zigzag BNNR-H and the zigzag BNNR, respectively, as drawn in Fig. 1(b) and 1(c). To produce the magnetism, some of B atoms in the three structures are substituted by carbon. Note that the boron substituted BNNTs have already been fabricated successfully in experiments. For example, Wei *et al.* prepared the carbon-substituted BNNTs by using electron-beam-induced doping strategy and confirmed that this class of nanotubes can exist stably even at room temperature.[40] In addition, the utilization of noncovalent interactions between dipolar molecules is also an effective route to introduce magnetism in these two nanostructures in experiment.[41,42]

To get comparable results, the three structures have the same numbers of B, N and C atoms in their unit cells. To avoid the interactions between carbon atoms in the repeated units, the every unit cell containing 40 atoms in the BNNT and the BNNR without any hydrogen passivation. The schematic structures of the thermal spin devices constructed by three parts, i.e., the central scattering regions with four repeated units, semi-infinite sources and drains as illustrated in Fig. 1. The number index in the right of Fig. 1(b) and 1(c) denotes the atom numbers along the y direction. Note that the y direction is perpendicular to the nanoribbons and the z direction is along the transport direction. T_L and T_R denote the device temperature in the source and the drain, respectively, and the spin-dependent currents can be produced by the temperature gradient $\Delta T(=T_L-T_R)$ between them without any external bias or back voltage.

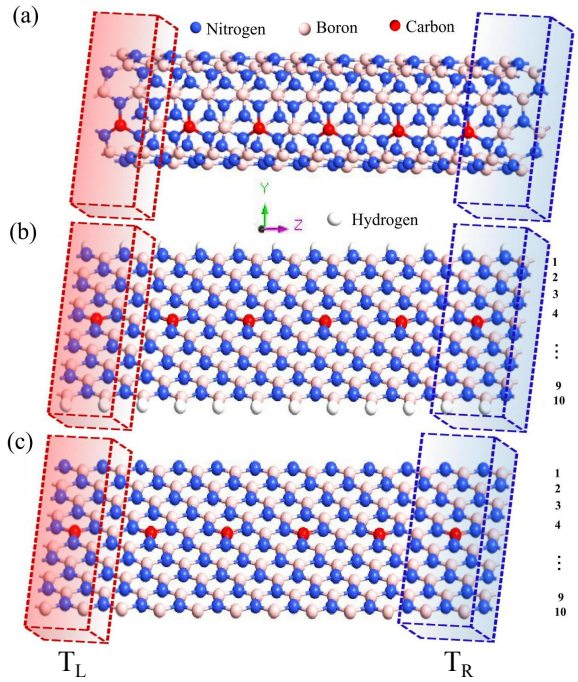

Fig. 1 (a)-(c) The schematic structures of thermal spin devices based on the carbon-substituting (5,5) amchair BNNT, 10-zBNNR-H and 10-zBNNR, respectively. Where the unit cells of the nanotube and the nanoribbons have the same numbers of the boron and nitrogen atoms. The red sphere stands for the lattice positions of the boron atoms substituted by carbon. The transport direction is defined as the z direction and the x axis is perpendicular to the plane, T_L and T_R denote the temperatures in the sources and the drains, and the temperature gradient between two contacts is defined as $\Delta T(=T_L-T_R>0)$.

The first-principle calculations on structural relaxation and band structures are performed in the frame of density function theory (DFT) with the spin generalized gradient approximation (SGGA) and Perdew-Burke-Ernzerhof (PBE) exchange correlation functional implemented in Atomistix ToolKit (ATK) Package.[43,44] The core electrons are described by norm-conserving pseudopotentials with the double numerical plus polarization (DNP) basis set. The cutoff energy is set as 75 Ry. Maximum force tolerance on each atom is 0.02 eV/Å and a $1\times5\times5$ Monkhorst-Pack k-point grid is adopted to the convergence of optimization. The spin-resolved transport spectra are calculated by using DFT together with non-equilibrium Green's function (NEGF) method[45,46], while the Double-Zeta-Polarized (DZP) and a $1\times1\times100$ Monkhors-Pack k-point grid are taken to obtain accurate results.[47]

Then the thermal spin-dependent currents (I_σ) through the device can be obtained by Landauer-Büttiker formalism[5,16]

$$I_\sigma=\frac{e}{h}\int_{-\infty}^{+\infty}T_\sigma(E)[f_L(E,T_L)-f_R(E,T_R)]dE, \quad (1)$$

This journal is © The Royal Society of Chemistry [year]

where e is the electronic charge, h is the Plank constant, and the equilibrium Fermi-Dirac distribution of the left (right) contact at temperature $T_{L(R)}$ is given by the equation $f_{L(R)}(E,T_{L(R)}) = [1+\exp(E-\mu_{L(R)})/k_BT_{L(R)}]^{-1}$. $\mu_{L(R)}$ is the chemical potential in the left (right) contact. The spin-resolved transmission coefficients of the devices can be calculated by using the non-equilibrium Green's function (NEGF) in the linear-resonance regime as $T_\sigma(E) = Tr[\Gamma_L G^R_\sigma(E)\Gamma_R G^A_\sigma(E)]$, where $\Gamma_{L/R} = i[\Sigma_{L/R} - \Sigma^+_{L/R}]$ indicates the interaction between a central scattering area and the left/right contact, whose self-energy is $\Sigma_{L/R}$. $G^{R/A}_\sigma(E)$ represents the retarded (advanced) spin Green's function of the central region, $G^R_\sigma(E) = [H^\sigma_c - (E+i\eta) + \Sigma_L + \Sigma_R]^{-1}$ and $G^A_\sigma(E) = [G^\sigma_R(E)]^\dagger$, here H^σ_c is the Hamiltonian in the central scattering region. Note that the temperature gradient ΔT produces the non-equilibrium Fermi-Dirac distributions in the source and drain to drive the thermal spin currents.

In the linear response regime, if ΔT approaches zero, we get $T = T_L \approx T_R$ and $\mu = \mu_L \approx \mu_R$ in the above thermal spin devices. Then, spin-dependent thermopower (S_σ), spin-dependent thermal conductance (k_σ) and spin-dependent electronic conductance (G_σ) can be calculated by[19]

$$S_\sigma(\mu,T) = -\frac{1}{eT}\frac{K_{\sigma,1}(\mu,T)}{K_{\sigma,0}(\mu,T)}, \tag{2}$$

$$k_\sigma(\mu,T) = \frac{1}{hT}[K_{\sigma,2}(\mu,T) - \frac{K^2_{\sigma,1}(\mu,T)}{K_{\sigma,0}(\mu,T)}], \tag{3}$$

$$G_\sigma = \frac{e^2}{h}K_{\sigma,0}, \tag{4}$$

where, $K_{\sigma,n}(\mu,T)$ is given by

$$K_{\sigma,n}(\mu,T) = -\int_{-\infty}^{+\infty}(E-\mu)^n\frac{\partial f(E,\mu,T)}{\partial E}T_\sigma(E)dE. \tag{5}$$

In addition, the phonon thermal conductance (k_{ph}) can be obtained by the Landauer-type formula as shown in the following[48]

$$k_{ph} = \frac{\hbar^2}{2\pi k_B T^2}\int_0^\infty d\omega[\omega^2 T_{ph}(\omega)\frac{e^{\hbar\omega/k_BT}}{(e^{\hbar\omega/k_BT}-1)^2}], \tag{6}$$

here, the phonon transmission function $T_{ph}(\omega)$ can be obtained by using DFT combined with the NEGF approach.

Finally, the figure of merit (ZT) to describe the TCE of the above-mentioned magnetic BNNT and BNNRs includes two terms, i.e., the charge figure of merit ($Z_{ch}T$) and spin figure of merit ($Z_{sp}T$), which are defined as[19]

$$Z_{ch(sp)}T = \frac{S^2_{ch(sp)}G_{ch(sp)}T}{k_e + k_{ph}}, \tag{7}$$

where $G_{ch} = G_{up} + G_{dn}$ and $G_{sp} = |G_{up} - G_{dn}|$ are the charge conductance and the spin one, respectively. $S_{ch} = (S_{up} + S_{dn})/2$ and $S_{sp} = S_{up} - S_{dn}$ are the charge- and spin-thermopower. $k_e = k_{up} + k_{dn}$ is the electronic thermal conductance. It should be noted that the Equations (2)-(6) are only valid at a small ΔT.

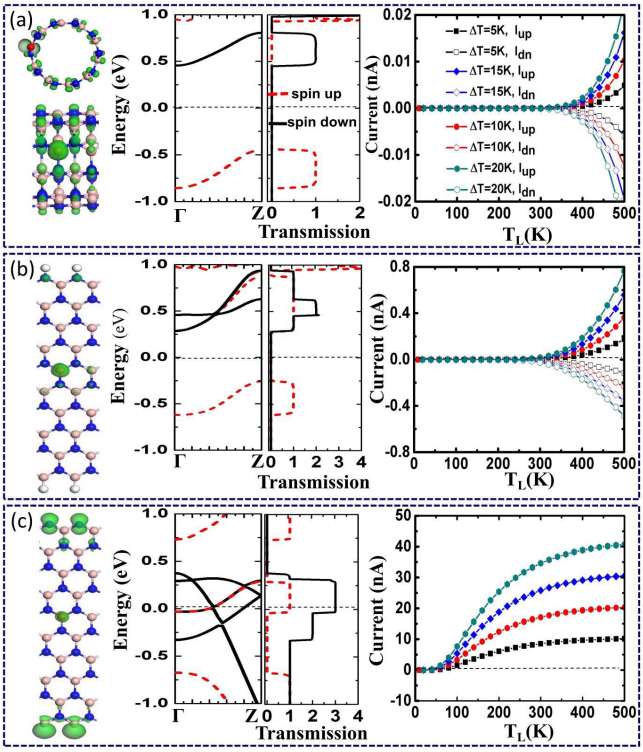

Fig. 2 (a)-(c) The spin density distribution with an isovalue of 0.05 eV/Å^3 (the left panels), the spin-dependent band structures, the spin-dependent transmissions (the central panels) and the thermally driven spin currents (the right panels) for the one-boron-substituted (5,5) armchair BNNT, 10-zBNNR-H and 10-zBNNR, respectively. Here, the unit cells of the nanoribbons and the nanotube are constituted by the same numbers of boron and nitrogen atoms, and we set the temperature gradient ΔT as 5, 10, 15 and 20 K. It is noted that I_{up} and I_{dn} are overlapped in Fig. 2(c).

3 Results and discussion

First of all, we should determine the magnetic states of the carbon-substituted BNNR and BNNT-H. In the latter, both edges have been passivated with hydrogen. The DFT calculations show that both structures display as the spin semiconducting state with nearly symmetrical spin-splitting band structures, as shown in Fig. 2(a) and 2(b), respectively. The particular electronic structures indicate that the nanotube and the nanoribbon can provide two symmetric spin-dependent spin channels, i.e., the spin-up channel below the Fermi level, and the spin-down one above the Fermi level. Their spin density distributions show that these two spin-dependent channels are contributed by the $2p$ electronic state in the carbon atoms. These spin-dependent transport channels suppose that these two samples can generate the nearly perfect SSE based on the conduction electrons, if a temperature bias is applied between the source and the drain. To illustrate this behavior, we calculate the thermally driven spin-up current (I_{up}) and spin-down current (I_{dn}) versus the device temperature T_L under some suitable values of ΔT, and plot the numerical results in the right panels of Fig. 2(a) and 2(b). One can find that I_{up} and I_{dn} have the opposite signs, indicating that they flow in the opposite directions in the transport channels with opposite spin directions, confirming the occurrence of the SSE.[49,50] Moreover,

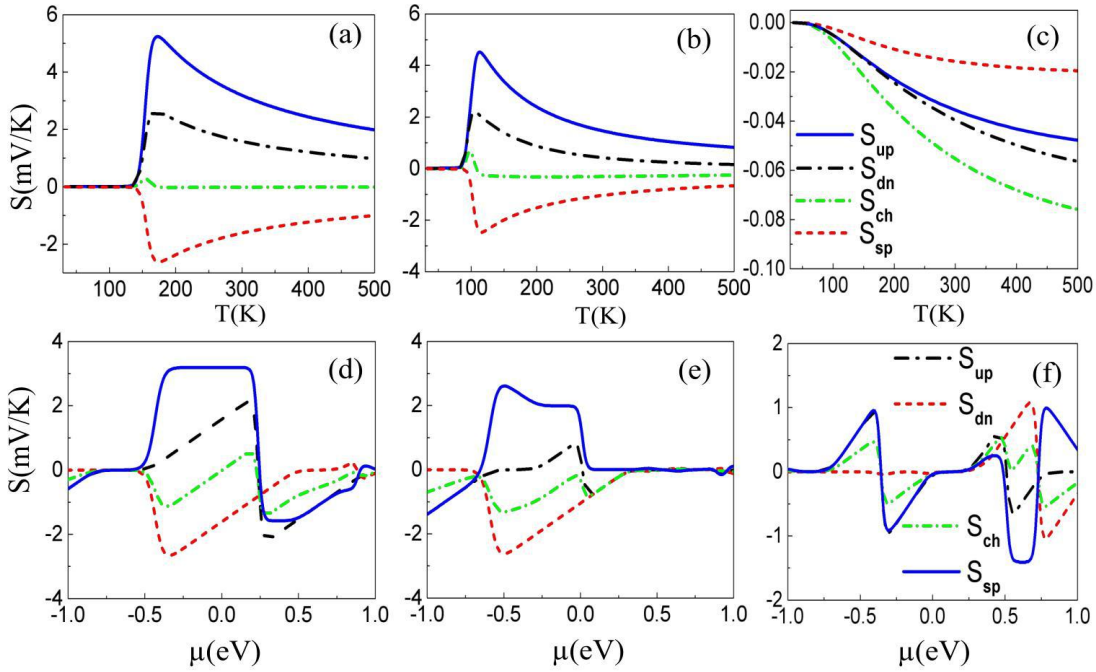

Fig. 3 (a)-(c) The spin-up thermopower S_{up}, spin-down thermopower S_{dn}, charge thermopower S_{ch} and spin thermopower S_{sp} versus the temperature T ($\approx T_L = T_R$) for the systems of one-boron-substituted (5,5) armchair BNNT, 10-zBNNR-H and 10-zBNNR, respectively. (d)-(f) S_{up}, S_{dn}, S_{ch} and S_{sp} as a function of the chemical potential μ for the corresponding systems.

although the SSE occurring in the different models constructed on the same quantum materials, yet there are two obvious differences as follows: (i) under the same conditions, the spin-dependent currents in the nanotube is smaller than those in the nanoribbon characterized by the fact that the threshold temperature in the former is higher than that in the latter, which is due to the larger band gap appearing in the nanotube; (ii) the symmetry of the spin-up and spin-down currents about the zero-current axis in the nanotube is higher than that in the nanoribbon due to an additional symmetry, i.e., the rotational symmetry,[51] appearing in the nanotube, which supports that the magnetic nanotubes can generate a better SSE in comparison with the related nanoribbons. These comparative studies give us deeper understandings into their respective advantages for these two different structures towards the thermal spin device applications. In particular, the rotational symmetry in the nanoscale systems should be taken into account as they are applied to generate the perfect SSE.

As the hydrogen passivation is removed from the above BNNR-H, we get another class of nanoribbon, i.e., the BNNR without any edge treatments, as drawn in Fig. 1(c). It is interesting that as the edge magnetism is produced, the magnetism originating from the carbons is suppressed largely, characterized by the comparable spin-state densities as plotted in Fig. 2(c). Apart from these, the electronic structures are changed remarkably, and the band structures show that this nanoribbon displays as a magnetic metallic state. Comparing with the previous one, i.e., BNNR-H, one can find that the metallic properties originate from the extended electronic states in both edges. Moreover, the transmission of the BNNR shows that this structure cannot generate any SSE, which is confirmed further by their thermally driven spin-dependent currents as shown in the right panel of Fig. 2(c). It can be concluded that the suitable edge treatment is a prerequisite to generate the SSE and other thermo-spin effects in the nanoribbons, and to make these effects to approach those of the related nanotubes constructed on the same quantum materials.

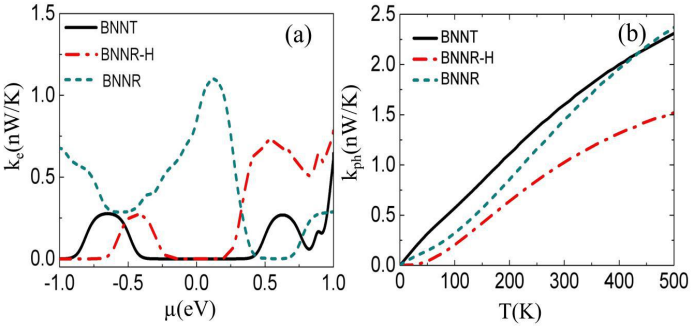

Fig. 4 (a) The electron thermal conductance k_e as a function of the chemical potential μ for one-boron-substituted (5,5) armchair BNNT, 10-zBNNR-H and 10-zBNNR, respectively. In the calculations, the temperatures in the three structures are set as 300 K. (b) The phonon thermal conductance k_{ph} versus T for the corresponding systems, which the chemical potential μ is set as zero.

The magnetic states and the spin transport characteristics influence their spin-related thermopower and other spin thermoelectric parameters remarkably. To study the spin-dependent thermoelectric properties, we limit our numerical calculation in the linear response regime and by adopting the approximation of nearly zero temperature bias, i.e., $T = T_L \approx T_R$. In Figs. 3(a)-(c), we plot the spin-up thermopower (S_{up}), the spin-down thermopower

This journal is © The Royal Society of Chemistry [year]

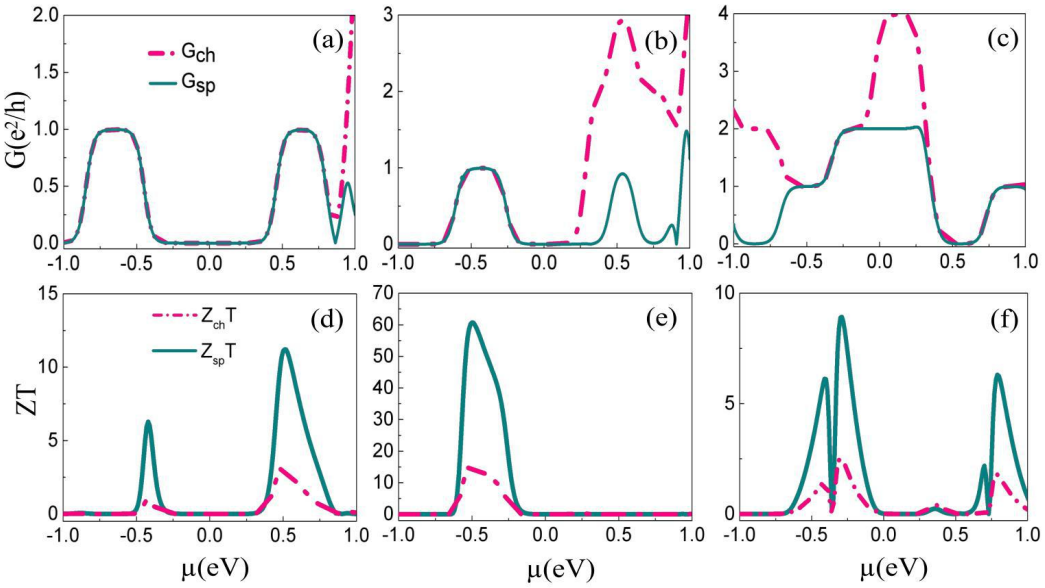

Fig. 5 (a)-(c) The spin-dependent conductance G as a function of the chemical potential μ for the systerms of one-boron-substituted (5,5) amchair BNNT, 10-zBNNR-H and 10-zBNNR, respectively. (d)-(f) The charge figure of merit $Z_{ch}T$ and spin figure of merit $Z_{sp}T$ versus the chemical potential μ for the systerms of one-boron-substituted (5,5) amchair BNNT, 10-zBNNR-H and 10-zBNNR, respectively.

(S_{dn}), the charge thermopower (S_{ch}) and spin thermopower (S_{sp}) as the device temperature T for the BNNT, the BNNR-H and the BNNT, respectively. As expected, for the structures of BNNT and BNNR-H, S_{up} and S_{dn} have the opposite signs, confirming further the occurring of the SSE in both structures. Meanwhile, the high symmetry of S_{up} and S_{dn} about the zero-thermopower axis suppresses S_{ch} to zero nearly in the whole temperature range, while the nonzero values of S_{ch} appear above the threshold temperature characterized by a small peak. Note that the peak of S_{ch} in the BNNT is smaller than the peak of S_{sp} in the BNNR-H, supporting that the SSE in the former is better than that in the latter. This is consistent well with the previous conclusion driven from the numerical results on the thermal spin-dependent currents. As for the second kind of the BNNR, the all thermopower coefficients behave as much small values, uncovering that the BNNR is not a good thermoelectric material. Furthermore, the relationship of the above four thermopower coefficients in these three structures with the chemical potential μ is also considered here. The numerical results show that the high symmetry of S_{up} and S_{dn} versus μ appears in the BNNT, while this symmetry is suppressed in the BNNT-H, and for the same values of μ, S_{up}, S_{dn} and S_{sp} in the BNNT are larger than the ones in the BNNR-H, as shown in Fig. 3(d) and 3(e). While for the BNNR, the all thermopower coefficients are zero in the Fermi level, which suppresses the thermopower largely. Besides, the higher symmetry of S_{up} and S_{dn} in the nanotube distributes around the Fermi level, while the potential value corresponding to the symmetric point of the thermopower in the nanoribbon shifts away from the Fermi level. These additional numerical calculations confirm further the previous conclusions.

To grasp the spin-dependent TCE, we should consider further the electric thermal conductance k_e and the phonon thermal conductance k_{ph} in these three materials. Fig. 4(a) shows k_e versus μ of these three different structures. One can find that under the same conditions, k_e in the nanotube is smaller than that in the nanoribbon, which is due to the fact that the larger band gap in the former suppresses the thermal electrons to transport through the device. Apart from this, the symmetry of k_e in the nanotube about $\mu = 0$ is much higher than that in the nanoribbon due to the rotational symmetry in the former. While for the BNNR, k_e is enhanced largely, even in the Fermi level, attributing to the metallic behaviors in both edges. Fig. 4(b) demonstrates k_{ph} versus the device temperatures of these three structures. One can find that under the same temperatures, k_{ph} in the nanotube is larger than the ones in both nanoribbons, displaying as an opposite changing trend comparing with the electron thermal conductance. In fact, the confinement effect in both edges induces the lattice phonon scattering in the nanoribbons. The nanotube, however, can be considered as a simple model of the nanoribbon having periodic boundary conditions, which suppresses the edge effect and reduces the phonon scattering largely. Considering that the phonon thermal conductance is contributed by the lattice vibrations, the larger values of k_{ph} appearing in the BNNT can be understood. Thus, we can find that comparing with nanoribbon structures, the nanotube has two oppositive influences on the thermal conductance. The advantage is to suppress electron thermal conductance due to the larger band gap, while the disadvantage is to enhance the phonon thermal conductance. In addition, as the passivated hydrogens are moved off, the phonon scattering in both edges is decreased, enhancing k_{ph} in the BNNR compared with the BNNR-H, as shown in Fig. 4(b). From the above comparative studies, the influence of the phonon scattering in the boundaries on k_e and k_{ph} should be fully taken into account as the nanoscale systems are applied in the therm-spin device applications.

As the charge conductance G_{ch} and the spin conductance G_{sp} are achieved, from equation (7), the characteristics of the TCE in the nanoscale structures can be analysed. In Figs. 5(a)-5(c), we plotted G_{ch} and G_{sp} versus μ for the BNNT, the BNNT-H and the BNNT, respectively. As expected, the main the changing tendency of G_{ch} in the nanotube and and nanoribbons is coincided with that of the related k_e as plotted in Fig. 4(a), since the low-temperature behaviors of G_{ch} is linearly proportional to k_e in the linear response regime.[19]. Meanwhile, the symmetry of G_{sp} about $\mu = 0$ is also determined by that of the spin-splitting bands of the system. The charge and spin figure of merit, i.e., $Z_{ch}T$ and $Z_{sp}T$, in these three structures are plotted in Fig. 5(d)-(f), respectively. It is obvious that $Z_{ch}T$ and $Z_{sp}T$ in the BNNT are characterized by the two nearly symmetric peaks localizing at $\mu = \pm 0.5$ eV, respectively. The maxima of $Z_{ch}T$ and $Z_{sp}T$ in the BNNR-H are larger than those of the previous one, however, both $Z_{ch}T$ and $Z_{sp}T$ have only one peak at $\mu = 0.5$ eV, losing the symmetry as showing in the BNNT. Recalling the previous studies on the thermopower and the thermal conductance, these differences in the TCE can be understood easily. The BNNT has the higher symmetry in the spin thermopower (see Fig. 3(d)) due to the rotational symmetry, while S_{up} and S_{dn} in the BNNR-H lose this symmetry (see Fig. 3(d)). As a result, ZT keeps zero in the positive-μ regime while the finite values appear in the negative-μ regime. Moreover, the BNNR-H has the lower thermal conductance, leading to the larger values in $Z_{ch}T$ and $Z_{sp}T$. In addition, $Z_{ch}T$ and $Z_{sp}T$ in the BNNT remains the typical behaviors of magnetic metals. It is concluded that the rotational symmetry and the phonon scattering in edges in nanoscale structures, as two important factors, should be taken into account when they are worked as the candidates to realize SSE with high spin figure of merit.

4 Conclusions

In summary, magnetic nanorribons and nanotubes are two potential structures to work as high-efficient spin caloritronics devices, to illustrate their respective advantages and disadvantages to realize the SSE with high spin figure of merit, we have constructed two nanoscale samples, i.e., the magnetic armchair BNNT and zigzag BNNR-H with the same magnetism origin, and studied the thermally driven spin currents and spin-dependent thermoelectric parameters symmetrically and comparatively. The theoretical results show that the two samples are spin semiconducting and can generate the SSE as a temperature gradient is applied along the samples. It is noted that the SSE in the former is much better than that in the latter, due to the rotational symmetry in nanotubes. Nevertheless, the spin-Seebeck currents in the BNNT are smaller than those in the BNNR-H, due to the larger band gap in the former. Moreover, the rotational symmetry in nanotubes leads to the nearly symmetric double-peak structure in the thermopower versus the onsite potential, and the losing of the rotational symmetry in nanoribbons leads to the single-peak structure in the thermopower of the BNNR-H. On the other side, due to the phonon scattering occurring in both edges of the BNNR-H, the phonon thermal conductance in the nanoribbons is smaller than that in the nanotubes, contributing to the enhancement of the charge and spin figure of merit of the systems.

In addition, we constructed another class of BNNT without any edge treatment for comparative studies, and found that the this kind of BNNT display as the spin thermoelectric behaviors of general metallic nanoribbons. Our results uncover that the rotational symmetry, the edge effect in boundaries and the hydrogen passivation in edges are three important factors to influence the SSE with high spin figure of merit in nanoscale systems, and provide us instructive routes to design the thermal spin devices nanotubes and nanorribons.

Conflicts of interest

There are no conflicts to declare.

Acknowledgements

This work is supported by the National Natural Science Foundation of China with grant No. 11774104 and 11274128. Work at UCI was supported by DOE-BES (Grant No. DE-FG02-05ER46237). Computer simulations were partially performed at the U.S. Department of Energy Supercomputer Facility (NERSC).

Notes and references

1 K. Uchida, S. Takahashi, K. Harii, J. Ieda, W. Koshibae, K. Ando, S. Maekawa and E. Saitoh, *Nature*, 2013, **102**, 554.
2 G. E. Bauer, E. Saitoh and B. J. van Wees, *Nat. Mater.*, 2010, **150**, 391–399.
3 S. Y. Huang, W. G. Wang, S. F. Lee, J. Kwo and C. L. Chien, *Phys. Rev. Lett.*, 2011, **107**, 216604.
4 G. J. Snyder and E. S. Toberer, *Nat. Mater.*, 2008, **7**, 105–114.
5 M. Zeng, Y. Feng and G. Liang, *Nano. Lett.*, 2011, **11**, 1369.
6 G. E. W. Bauer, E. Saitoh and B. J. van Wees, *Nat. Mater.*, 2012, **11**, 391–399.
7 S. R. Boona, R. C. Myers and J. P. Heremans, *Ene. Envir. Sci.*, 2014, **7**, 885–910.
8 D. Hirobe, M. Sato, T. Kawamata, Y. Shiomi, K. Uchida, R. Iguchi, Y. Koike, S. Maekawa and E. Saitoh, *Nat. Phys.*, 2016, **13**, 30–34.
9 L. Gu, H.-H. Fu and R. Wu, *Phys. Rev. B: Condens. Matter*, 2016, **94**, 115433.
10 L. J. Cornelissen, J. Liu, R. A. Duine, J. B. Youssef and B. J. V. Wees, *Nat. Phys.*, 2015, **11**, 146–50.
11 Y. Kajiwara, K. Harii, S. Takahashi, J. Ohe, K. Uchida, M. Mizuguchi, H. Umezawa, H. Kawai, K. Ando and K. Takanashi, *Nature*, 2010, **464**, 262–6.
12 Y. C. Otani, M. Shiraishi, A. Oiwa, E. Saitoh and S. Murakami, *Nat. Phys.*, 2017, **13**, 829–832.
13 T. Kimura, Y. Otani, T. Sato, S. Takahashi and S. Maekawa, *Phys. Rev. Lett.*, 2007, **98**, 156601.
14 S. O. Valenzuela and M. Tinkham, *Nature*, 2006, **442**, 176–179.
15 H.-H. Fu, D.-D. Wu, L. Gu, M. Wu and R. Wu, *Phys. Rev. B: Condens. Matter*, 2015, **92**, 045418.
16 M. Zeng, W. Huang and G. Liang, *Nanoscale*, 2012, **5**, 200–208.
17 L. E. Bell, *Science*, 2008, **321**, 1457–1461.

This journal is © The Royal Society of Chemistry [year]

18 F. J. DiSalvo, *Science*, 1999, **285**, 703–706.

19 L. D. Hicks and M. S. Dresselhaus, *Phys. Rev. B: Condens. Matter*, 1993, **47**, 12727.

20 L. D. Hicks and M. S. Dresselhaus, *Phys. Rev. B: Condens. Matter*, 1993, **47**, 16631.

21 G. Zhou, L. Li and G. H. Li, *Appl. Phys. Lett.*, 2010, **97**, 787.

22 H. Zheng, H. J. Liu, X. J. Tan and H. Y. Lv, *Appl. Phys. Lett.*, 2012, **100**, 12727.

23 D. D. Fan, L. Cheng, P. H. Jiang, J. Shi and X. F. Tang, *Appl. Phys. Lett.*, 2014, **105**, 133113.

24 P. Jiang, X. Tao, H. Hao, L. Song, X. Zheng, L. Zhang and Z. Zeng, *2D Mater.*, 2017, **4**, 035001.

25 R. R. Nair, I. L. Tsai, M. Sepioni, O. Lehtinen, J. Keinonen, A. V. Krasheninnikov, A. N. Castro, M. I. Katsnelson, A. K. Geim and I. V. Grigorieva, *Nat. Commun.*, 2013, **4**, 2010.

26 D. Naveh and A. Ramasubramaniam, *Phys. Rev. B: Condens. Matter*, 2013, **87**, 2624–2628.

27 A. K. Singh, T. M. Briere, V. Kumar and Y. Kawazoe, *Phys. Rev. Lett.*, 2003, **91**, 146802.

28 Z.-Q. Zhang, Y.-R. Yang, H.-H. Fu and R. Wu, *Nanotechnology*, 2016, **27**, 505201.

29 M. Wu, S. Dong, K. Yao, J. Liu and X. C. Zeng, *Nano Lett.*, 2016, **16**, 7309–7315.

30 H.-H. Fu, L. Gu and D.-D. Wu, *Phys. Chem. Chem. Phys.*, 2016, **18**, 12742–12747.

31 D.-D. Wu, H.-H. Fu, L. Gu, Y. Ni, F.-X. Zu and K.-L. Yao, *Phys. Chem. Chem. Phys.*, 2014, **16**, 17493–17498.

32 L. Weston, D. Wickramaratne, M. Mackoit, A. Alkauskas and C. G. V. de Walle, *Phys. Rev. B: Condens. Matter*, 2018, **97**, 214104.

33 R. Q. Wu, L. Liu, G. W. Peng and Y. P. Feng, *Appl. Phys. Lett.*, 2005, **86**, 716.

34 M. Kan, Y. Li and Q. Sun, *Wires. Comput. Mol. Sci.*, 2016, **6**, 65–82.

35 W. Q. Han, H. G. Yu and Z. Liu, *Appl Phys Lett.*, 2011, **98**, 411.

36 T. W. Lin, C. Y. Su, X. Q. Zhang, W. Zhang, Y. H. Lee, C. W. Chu, H. Y. Lin, M. T. Chang, F. R. Chen and L. J. Li, *Small*, 2012, **8**, 1384–1391.

37 Z. Song, Z. Li, H. Wang, X. Bai, W. Wang, H. Du, S. Liu, C. Wang, J. Han and Y. Yang, *Nano Lett.*, 2017, **17**, 2079–2087.

38 V. Meunier, A. G. Souza Filho, E. B. Barros and M. S. Dresselhaus, *Rev. Mod. Phys.*, 2016, **88**, 025005.

39 N. T. Hung, A. R. T. Nugraha, E. H. Hasdeo, M. S. Dresselhaus and R. Saito, *Phys. Rev. B: Condens. Matter*, 2015, **92**, 165426.

40 X. Wei, M. S. Wang, Y. Bando and D. Golberg, *J. Am. Chem. Soc.*, 2010, **132**, 13592–13593.

41 Y. Lee, S. Kim, C. Park, J. Ihm and Y. Son, *ACS Nano*, 2010, **4**, 1345–1350.

42 B. M. Wong, S. H. Ye and G. O'Bryan, *Nanoscale*, 2012, **4**, 1321–1327.

43 J. Taylor, H. Guo and J. Wang, *Phys. Rev. B: Condens. Matter*, 2001, **63**, 245407.

44 *Atomistix ToolKit*, `http://quantumwise.com/`.

45 H.-H. Fu and K.-L. Yao, *Appl. Phys. Lett.*, 2012, **100**, 1348.

46 H.-H. Fu, K.-L. Yao and Z.-L. Liu, *J. Chem. Phys.*, 2008, **129**, 134706.

47 Y. Imry and R. Landauer, *Rev. Mod. Phys.*, 1999, **71**, 515–525.

48 K. K. Saha, T. Markussen, K. S. Thygesen and B. K. Nikolic, *Phys. Rev. B: Condens. Matter*, 2011, **84**, 041412(R).

49 D.-D. Wu, Q.-B. Liu, H.-H. Fu and R. Wu, *Nanoscale*, 2017, **9**, 18334–18342.

50 M. G. Zeng, Y. P. Feng and G. C. Liang, *Nano Lett.*, 2011, **11**, 1369–1373.

51 Y. Wang, J. Xu, Y. W. Wang and H. Y. Chen, *Chem. Sco. Rev.*, 2013, **42**, 2930–2962.